 doi:10.20944/preprints202208.0216.v1

Article

Modelling of Soil Spatial Variability in an Olive Grove by Fusing Remote Drone-based Multispectral Data, Ground-based Hyperspectral and Sample Data with Multivariate Geostatistics Taking into Account Change of Support

Antonella Belmonte [1], Carmela Riefolo [2,*], Lovergine Francesco [1] and Annamaria Castrignanò [3]

[1] Institute for Electromagnetic Sensing of the Environment, National Research Council (CNR-IREA), via Amendola 122/D, 70126 Bari, Italy; belmonte.a@irea.cnr.it (A.B.); lovergine.f@irea.cnr.it (F.L.)
[2] CREA-AA—Council for Agricultural Research and Economics, Via Celso Ulpiani, 5, 70125 Bari, Italy 2
[3] Department of Engineering and Geology (InGeo), Gabriele D'Annunzio University of Chieti-Pescara, 66013 Chieti, Italy; annamaria.castrignano@unich.it (A.C.)
* Correspondence: carmela.riefolo@crea.gov.it

Abstract: Traditional soil characterization methods are time consuming, laborious and invasive and do not allow long-term repeatability of measurements. The overall aim of this paper was to assess and model spatial variability of the soil in an olive grove in south Italy by using data from two sensors of different type: a multi-spectral on-board drone radiometer and a hyperspectral visible-near infrared-shortwave infrared (VIS-NIR-SWIR) reflectance radiometer as well as sample data, to arrive at a delineation of homogeneous areas. The hyperspectral data were processed using continuum removal methodology to obtain information about the content and composition of clay. Differently, the multispectral data were firstly upscaled to the support of soil data using geostatistics and taking into account change of support. Secondly, the two-sensor data were integrated with soil granulometric properties by using the multivariate geostatistical techniques of multi-collocated cokriging and factor cokriging, in order to achieve a more exhaustive and finer-scale soil characterisation. The paper shows the impact of change of support on the uncertainty of soil prediction that can have a significant effect on decision making in Precision Agriculture. Moreover, four regionalised factors at two different scales (two per each scale) were retained and mapped. Each factor provided a different delineation of the field with areas characterised by different granulometry and clay composition. The applied method is sufficiently flexible and could be applied to any number and type of sensors.

Keywords: block cokriging; clay composition; granulometry; multi-collocated cokriging; multi-collocated factorial cokriging; regularization; SIDSAM; VIS-NIR-SWIR spectroscopy

1. Introduction

In recent years, agriculture has been undergoing a profound revolution, moving from an era characterised by widespread and capillary mechanisation to one based on intensive and diffuse use of information. It is this era that is seeing an increasing use of precision agriculture (PA), which is based on optimising agronomic inputs at a small within-field scale to achieve the following main objectives: increased production and product quality/safety, with resulting gains in profitability, and reduced environmental impact with improved sustainability. It is therefore a much more complex way of making agriculture than in the past, the success of which depends strongly on the efficiency and reliability of the methods used to collect site-specific within-field information and process this large amount of data. PA could then be defined as an information and computation intensive technology [1].

 doi:10.20944/preprints202208.0216.v1

Among the various components of an agricultural system, soil is undoubtedly one of the most important due to its significant impact on plant growth, yield and product quality/safety. Farmers have always been well aware of this, since for centuries they have been using soil information to make their agronomic management decisions. Traditionally, soil information has been collected with grid sampling at both regional and local scales. While this method has produced useful results in the past, it currently shows all its limitations in modern agriculture, having its disadvantages. First, sampling costs increase exponentially as the grid mesh decreases. In addition, the information obtained with sampling is inevitably sparse, i.e., it is not available at every point in the field. To make it exhaustive, it would be necessary to apply some interpolation method, but this introduces an error. It follows from the above that, in order to make informed operational decisions in PA, it is necessary to have soil information at a very fine even sub-metric scale, which would make grid sampling almost impractical. One way to solve this problem is to integrate the limited soil information from sampling with the higher spatial density information provided by remote and proximal sensing. The difference between remote (RS) and proximal (PS) sensing lies in the distance between the sensor and the target object: while RS measurements are non-contact, PS measurements refer to on-the-go ones on the surface or at a height of no more than 2m [2]. Many studies have used RS images of bare soil and soil reflectance to map and quantitatively characterize soil attributes [3–6]. Compared to traditional methods, such as the pipette method for soil granulometry determination, RS has proven to be undoubtedly cheaper and quite accurate at least for certain applications. Images of bare soil from satellite or aircraft allow to cover large areas even with a sufficient degree of spatial detail. However, they may present certain limitations when applied in PA. Although the spatial resolution of satellite products has improved a lot in recent years to the metric scale, such as commercially offered by EOS (Earth Observation System, ww.eos.com), this may not be sufficient in PA where centimetric spatial resolution is sometimes required. For example, it is necessary to supplement cultivation models based on aerial images of the crop with much finer resolution soil data [7]. Furthermore, in order to be able to intervene promptly with some agronomic operation, it is necessary to have an on-time record of the state of the crop and/or soil. Aerial measurements from a drone (UAV) make it possible to obtain images of soil or crop at a centimetric spatial resolution and at the time desired by the farmer. This explains the increasing use of drones for PA in recent times also in combination with lower prices and fewer restrictions on flight authorisation.

Although the use of hyperspectral radiometers on board drones is becoming increasingly popular, it is currently not yet common in PA, due to both the still high costs and the complexity of signal processing. It therefore follows that the degree of spectral information of the soil from remote images remains rather low. Multispectral images with low spectral density often limit interpretation to essentially qualitative determinations of soil.

On the other hand, spectroscopic reflectance measurements on soil samples obtained in laboratory allow quantitative determinations of soil properties. It has now become common laboratory practice for soil analytical measurements. However, hyperspectral data captured with spectrometers are generally noisy and difficult to interpret even under well-controlled laboratory conditions. It is therefore extremely critical to use appropriate procedures for both data pre-processing and analysis. Currently two distinct estimation techniques are widely applied to characterize qualitative and quantitative soil attributes: chemometric techniques by regression models and Continuum Removal (CR) [8].

While pretreatment methods are required for the former to correct baseline shifts in reflectance spectra across the wavelength range due to the scattering effect [9–10], CR is a normalization treatment of spectra which only concerns those absorption regions to be compared against a common baseline [11]. This technique has the advantage of identifying specific absorption features that should persist at different observation conditions. In addition, CR technique is easier to perform than chemometric techniques.

After the application of CR method, intensity values of absorption at specific bands can be calculated from VNIR-SWIR spectra to estimate minerals, rocks and some soil

 doi:10.20944/preprints202208.0216.v1

properties. The absorption characteristics of several minerals, including clay and CaCO3, have been extensively studied using this technique both under laboratory conditions [12] and from remotely sensed data [13].

Soil samples for lab spectroscopic analysis are usually collected with grid sampling, which inevitably limits their number. All of the above leads to the statement that there is no single sensor capable of providing accurate measurements of all soil properties. To improve the accuracy of spatial predictions, a successful approach may be to use several different sensors in addition to direct laboratory measurements of soil attributes, a process called data fusion [14–16]. This is by no means a trivial problem since it involves jointly analysing heterogeneous multi-source spatial data with different statistical properties and spatial resolution [17–18]. Furthermore, when delineating management zones in PA, predictions are made at a higher level of spatial association than the one of the original data (upscaling). This process known as change of support [19–21] reduces spatial heterogeneity and estimate uncertainty by producing a smoothing effect. Geostatistics offers various solutions to the change of support problem specifically in PA. Block cokriging and block factor cokriging for partitioning field into homogeneous sub-field areas are the traditional geostatistical techniques used to treat the change of support problem. The advantages of using geostatistics derive from the fact that it explicitly takes into account the spatial correlation between observations and allows the reduction in uncertainty, due to upscaling, to be evaluated quantitatively.

The objective of this work is the definition of a geostatistical approach of multi-spectral drone soil data fusion with hyperspectral ground-based data and laboratory granulometry measurements for field delineation in homogeneous areas, which allows to estimate the uncertainty reduction due to scale change.

2. Materials and Methods

2.1. Soil sampling and study site

The sampling was carried out in an olive grove of 100-year-old trees of the Ogliarola Salentina cultivar in July 2019, located in Oria (province of Brindisi, South-East of Italy). Three topsoil samples (0-0.20 m) were collected near the plants, and then dried, ground, sieved to 2 mm and mixed in laboratory to obtain a single sample per each tree. The field is flat and skeleton free. The soil was classified as Calcic Haploxeralf, fine, mixed, thermic (USDA, 1999), which I is widespread in Mediterranean areas where grapes and olives are cultivated, and remains dry for long periods in summer. The term "Haploxeralf" involves a loamy granulometry and a relatively thin argillic or kandic horizon, whereas "Calcic" regards a calcic horizon with its upper boundary within 1 m of the mineral soil surface. Since in this study a topsoil (0-0.20 m) was surveyed, this characteristic is not quite relevant.

2.2. Drone data

The images were acquired from a multispectral sensor mounted on a multi-rotor DJI Mavic Pro drone. The platform had a total payload mass of ~800 g, and a flight range of ~7 km [36] (Castrignanò et al., 2020). The camera (Parrot Sequoia) allowed acquiring multispectral images at high-resolution (0.07 m) from an altitude of 70 m and with the sampling distance (GSD) of 0.066 m/pixel.

The characteristics of multispectral sensor are reported in the Table 1.

Preprints (www.preprints.org) | NOT PEER-REVIEWED | Posted: 11 August 2022 doi:10.20944/preprints202208.0216.v1

Table 1. Properties of the multispectral sensor Parrot Sequoia.

Camera resolution	Image size		Bands	Mass	Size
1.2 Mpx*	1280 x 960	pixels	Green (550 ± 20 nm) Red (660 ± 20 nm) Red Edge (735 ± 5 nm) NIR (790 ± 20 nm)	72 g	59 x 41 x 28 mm

*Mpx (Megapixel) is equivalent to one million pixels.

The acquisitions were done using the typical aerial-mapping "serpentine" profile (Fig. 1a) with planned overlap and 80% sidelap.

All of the spectral datasets were processed with Pix4d Mapper 4.4.12 software applying photogrammetric techniques, to create a quoted point cloud for 3D reconstruction and an orthophoto image for each band as final result (Fig. 1b).

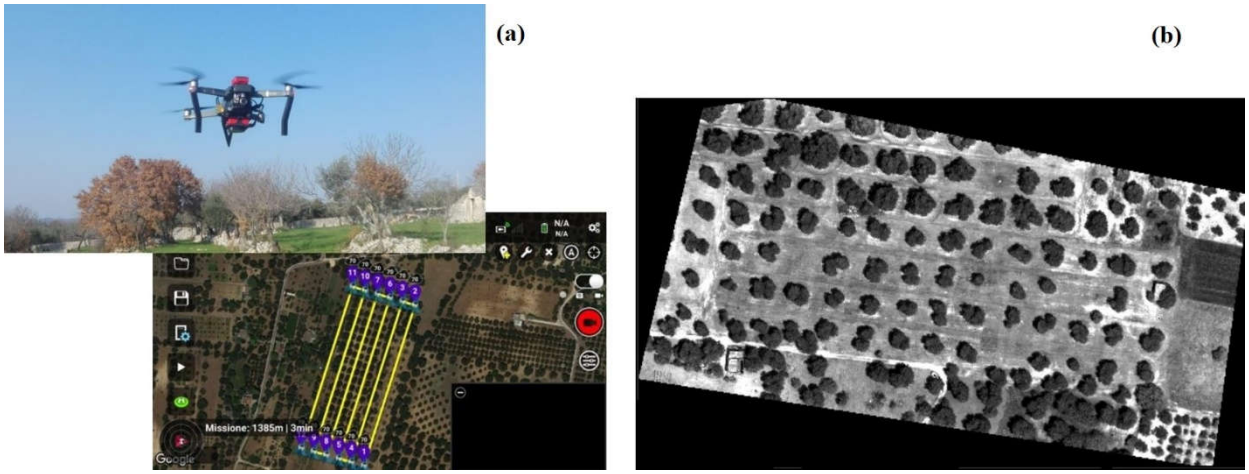

Figure 1. The multi-rotor DJI Mavic Pro drone and its flight plan (a), an example of orthophoto image (green band) (b).

The drone image had previously been classified in three classes (crown, shadow and soil) (Castrignanò et al., 2020). The classification product was then cut using the polygon shapefile of the field boundary (Oria-RE). In the following there is the description of the different steps of the applied methodology for extracting soil pixels alone from the drone image:

1. Recombining classes & mask generation

In this step the procedure 'combine classes' of the commercial ENVI (ENvironment for Visualizing Images) 5.1 software (Harris Geospatial) was applied. In this way, two classes (crown and shadow) were merged into one class 'not-soil' and then the corresponding binary image (not soil 0, soil 1) was extracted.

2. Point shapefile of soil

Four point shapefiles containing soil information were extracted from each drone band using the tool (r.tovector) of the Grass (Geographic Resources Analysis Support System) module integrated in the open source QGIS 3.22.1 software (Quantum Geographic Information System).

3. CSV file

To use soil drone data in the in the subsequent geostatistical analysis, the point shapefile was converted in CSV format. This step was performed by applying the plugin MMQGIS in QGIS.

Preprints (www.preprints.org) | NOT PEER-REVIEWED | Posted: 11 August 2022 doi:10.20944/preprints202208.0216.v1

The methodology to extract the soil information from drone data is shown in the following flowchart (see Fig. 2).

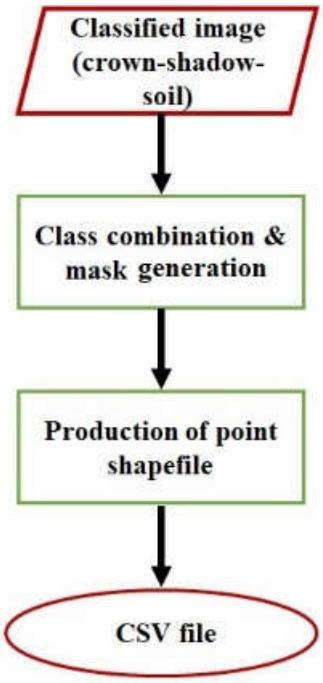

Figure 2. Flow Chart of automatic extraction of soil information from drone data.

2.3. Laboratory-based granulometry measurement

The granulometric determinations were based on taking the suspension of particles with diameters less than 200 μm at different heights and at predetermined times according to pipette method [22–23]. The following soil particle size fractions (%) were determined directly: coarse sand (2.0-0.2 mm), silt (0.05-0.002 mm) and clay (<0.002 mm). The fine sand (0.2-0.05 mm) was calculated as the complement to 100 of the previous components. Total sand was calculated as the sum of coarse and fine sand.

2.4. Hyperspectral data and their analysis

VIS-NIR-SWIR reflectance of the soil samples was measured with ASD FieldSpec IV spectroradiometer (Analytical Spectral Devices Inc., Boulder, Colorado, USA) over 350–2500 nm spectral range in the same conditions described in the work of Riefolo et al. 2022 [24].

The raw data over the whole spectral range had been elaborated with Principal Component Analysis in a previous paper [24] and the retained components (PCs) were elaborated with Continuum Removal (CR) in the ranges around 1400, 1900, 2200 nm, to assess the influence of clay composition (illite (1400 nm), montmorillonite (1900 nm), kaolinite (2200 nm) on PCs' structure. The interested reader is referred to the aforementioned paper for a more detailed description of these procedures. In this paper it is only pointed out that they were used to characterise the composition of the clay. Moreover, the Depth parameters previously calculated at 1400 nm (D1400) and at 1900 nm (D1900) were normalized respect to the parameter Depth at 2200 m (D2200). Therefore, the following ratios: R1= D1400/D2200 and R2= D1900/D2200 were calculated and discussed in this work. On how these parameters were determined, the interested reader can refer to the previously mentioned work. Here, only how these parameters relate spatially to other soil variables, in particular the granulometric components, will be discussed.

To facilitate the interpretation of the results, it is only mentioned that the three retained PCs cumulatively explained a proportion of the variance greater than 98%, more

Preprints (www.preprints.org) | NOT PEER-REVIEWED | Posted: 11 August 2022 doi:10.20944/preprints202208.0216.v1

particularly PC1 explained the 92.2%, PC2 4% and PC3 2% of total variance. PC1, due to the high proportion of variance explained, was assigned the meaning of an indicator of the average soil reflectance integrated over the full spectrum (350nm - 2500nm). Furthermore, PC1 was related to clay component called illite. PC2 to clay component called montmorillonite and PC3 to iron oxides, specifically to geothite in the range of 370-440 nm.

2.5. Spectral Index of soil samples

In the work of Riefolo et al. 2022 [24] different spectral methods (Spectral Angle Mapping SAM, Spectral Information Divergence (SID) and SIDSAM, [25] were applied to compare the spectral properties of the soil samples respect to the ones of the maximum reflectance sample assumed as reference. In this study only SIDSAM was used as it integrates the deterministic (SAM) and stochastic (SID) characteristics of the two previously mentioned indices. Moreover, SIDSAM improves the power of discriminating one spectrum from a reference spectrum [25].

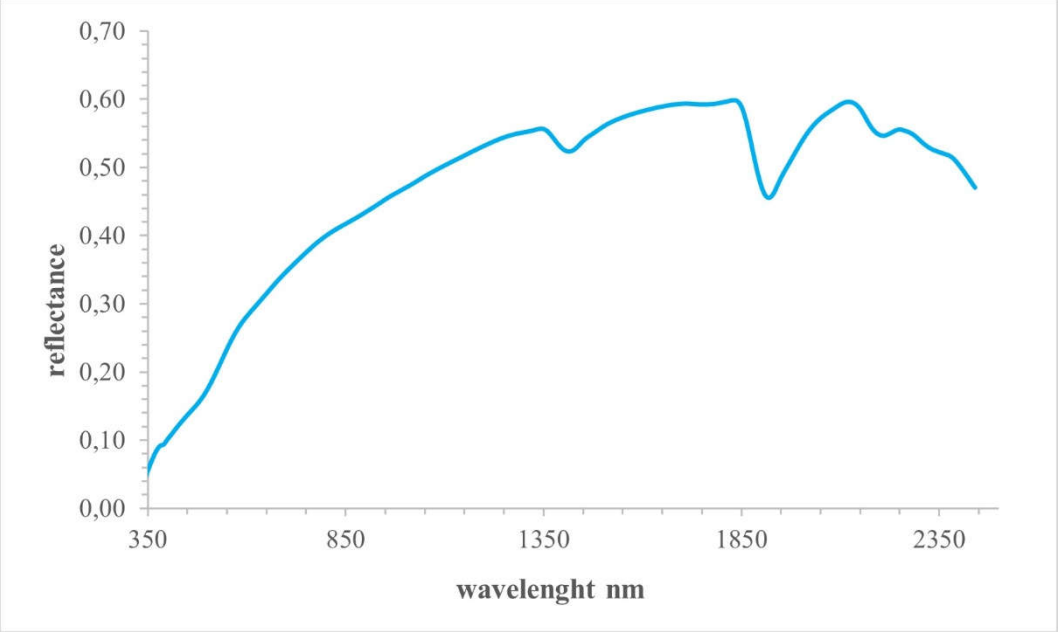

Figure 3. Graph of most reflective spectrum, chosen as the reference one in the olive grove.

In Fig. 3 the most reflective spectrum is shown with the characteristic absorption bands at 1400, 1900 and 2200 nm associated with the presence of illite, montmorillonite and kaolinite, respectively, and observed also in all the other spectra collected at sample locations (data not shown).

2.6. Geostatistical procedures

Firstly, exploratory data analysis was performed to calculate the basic statistics of the study variables including mean, median, minimum and maximum values, standard deviation, skewness and kurtosis.

If the data distributions appeared asymmetrical with skewness coefficient greater than 1, the variables were transformed into standardised Gaussian variables with mean 0 and variance 1, before performing multivariate geostatistical analysis. For this purpose, a Hermite polynomial series was used and the approach is called Gaussian Anamorphosis [26,27].

Therefore, all geostatistical procedures were performed in the Gaussian domain, and only at the end the estimates were back-transformed to the raw data by using the fitted anamorphosis model.

Preprints (www.preprints.org) | NOT PEER-REVIEWED | Posted: 11 August 2022 doi:10.20944/preprints202208.0216.v1

The multivariate data sets, both the one containing only drone data and the combined one resulting from the fusion of multi-band drone data, hyperspectral data and soil granulometric measurements, were spatially modelled under the scope of the linear model of coregionalization (LMC) [28,26]. LMC considers the study variables as generated by the same independent physical processes acting over N_s different spatial scales. All experimental direct and cross-variograms were then jointly modelled as linear combinations of the same set of N_s basic variograms $g^u(\boldsymbol{h})$ for each spatial scale u standardized to sill 1:

$$\gamma_{ij}(\mathbf{h}) = \sum_{u=1}^{Ns} b_{ij}^u g^u(\mathbf{h}) \quad (1)$$

$$i, j = 1,\ldots, p$$

where $\gamma_{ij}(\mathbf{h})$ is the cross-variogram model between variables Z_i and Z_j; $\boldsymbol{h}$ is a distance vector, called lag, and b_{ij}^u are the partial sills of the variograms $g^u(\boldsymbol{h})$, specific for each pair of variables i and j and for each spatial scale u.

By assembling all b_{ij}^u coefficients related to a specific scale u, a symmetric $\mathbf{B^u}$ matrix is determined, which is called coregionalisation matrix. This could be considered as the analogue of the variance-covariance matrix but for a specific scale u. Therefore, according to the LMC perspective, the variance-covariance matrix could be decomposed into the sum of the coregionalisation matrices relating to Ns spatial scales [29]. Fitting of LMC was performed with weighted least-squares method under the constraint of positive semi-definiteness of the $\mathbf{B}^u$ by using an iterative approach developed by Rivoirard (2001) [30]. The results were evaluated with cross-validation techniques [31] using mean and variance of the standardised error (SE) against the cokriging standard deviation as error statistics [32]. The optimal values of the two statistics should be 0 and 1, respectively.

2.8. Change of support

Geostatistical techniques were used to model the effects of change of scale when estimates are calculated on an area / volume (support) bigger than the one of observations. This was obtained through the geostatistical operation of regularization, which provides a tool to re-scale the statistics and spatial functions (covariance, variogram) that describe the data rather than rescale the data themselves [33].

The point support was assumed to be that of multispectral drone data (0.07m x 0.07m), while the estimates were obtained on a 1m x 1m block, which was the characteristic support for the measurements on the ground. The point variograms were then transformed into the corresponding variograms on the block support by discretizing the blocks into equal cells with a fixed mesh size (0.10 m). After that, pseudo-point experimental variograms were calculated in the fictitious cell centers within the block and then the point variograms were averaged (regularized) over the block. This change of support of the drone data was necessary in order to fuse heterogeneous data (multi-band drone, hyperspectral and granulometric data) in the multivariate geostatistical analysis.

To provide the estimates of multi-spectral drone data on 1m-by-1m block support, block cokriging was applied which is one of the traditional geostatistical interpolation methods to solve the change of support problem [34,35,27]. It allows to predict the variables at a scale larger than the one of observation through the process of regularization as described before. Block support variograms of drone data were then calculated from point support variograms to provide mean estimates on a 1-m mesh grid [36]. It is worth underlining as block cokriging allows to refer the estimates of different variables to the same support (block), so solving the crucial problem of combining sensor data with different spatial resolution [37].

Preprints (www.preprints.org) | NOT PEER-REVIEWED | Posted: 11 August 2022 doi:10.20944/preprints202208.0216.v1

2.9. Data Fusion and partitioning of the field

2.9.1. Multi-collocated cokriging

Cokriging is the traditional multivariate estimator in geostatistics which enables to improve the accuracy of poorly sampled variables by using more densely sampled auxiliary variables [38,39].

In particular, the variant multi-collocated cokriging was used in this work to fuse sparse primary variables with gridded auxiliary variables. Multi-collocated cokriging [30] is a simplified version of full cokriging, which makes use of the much more densely sampled auxiliary variable(s) only at the target point and at all locations where the primary variable(s) of interest is(are) available [40]. This approach requires that the auxiliary variable(s) is(are) known at all nodes of the interpolation grid besides at the locations where the interest variable(s) is(are) measured. This approach is particularly useful when the auxiliary variables are particularly redundant (raster variables), whereby the use of the full neighborhood for interpolation would cause the inversion of the matrices to be very time-consuming or even impossible [26,27].

In this work, the multi-band drone variables were first interpolated onto a 1 m mesh grid with block cokriging and then assumed as auxiliary grid variables in the application of multi-collocated cokriging to the complete fusion data set.

2.9.2. Multi-collocated cokriging

The same LMC fitted for the fusion data set was used in multi-collocated fctorial cokriging analysis to extract few synthetic scale-dependent indicators to be used for field partition. Factorial cokriging is a geostatistical technique for assessing and modelling the spatial correlations of a multivariate spatial dataset at the different scales, developed by Matheron (1982) [41]. Besides LMC fitting, it consists of two additional steps: (i) analyzing the correlation structure of variables at each scale by applying traditional principal component analysis (PCA) on the corresponding coregionalization matrix, to extract a set of orthogonal components known as scale-dependent regionalized factors; and (ii) cokriging and mapping regionalized factors by solving a modified cokriging system [26]. The variant multi-collocated factor cokriging was used in the same manner as illustrated earlier. It is worth underlining that regionalised factors are but mathematical constructions with no prior physical meaning [29], therefore they were interpreted on the basis of the prevalent loading coefficients in their formulation.

2.10. Estimation uncertainty

Estimation uncertainty of the granulometric variables (silt, clay), which were the target variables of this work, was assessed by calculating the confidence interval (95%CI), which provides the range of variation of the estimate at each node of the interpolation grid with an error less than or equal to 5%. [36]. The upper and lower 95%CI limits pertaining to the gaussian estimate were calculated by summing or subtracting 1.96 cokriging standard deviation to the estimate, respectively. Upper and lower limits and estimate of gaussian transformed variables were then back-transformed to the raw data by using the gaussian anamorphosis model, previously fitted. This made it possible to calculate the estimation uncertainty of even strongly skewed variables.

3. Results and discussion

3.1. Geostatistical analysis of Drone data and change of support

From the original drone image 2,032,972 pixels were extracted attributable to soil and in Table 2 the basic statistics of the four band soil reflectance are reported. All four variables showed a skewness coefficient greater than 1, which means that the data distributions were asymmetric due to the presence of numerous large outliers.

Preprints (www.preprints.org) | NOT PEER-REVIEWED | Posted: 11 August 2022 doi:10.20944/preprints202208.0216.v1

Table 2. Basic statistics of the four band drone reflectance.

Variable	Minimum	Maximum	Mean	Median	Std. Dev.	Skewness	Kurtosis
green	0.027	0.256	0.098	0.094	0.018	1.56	7.73
Red	0.021	0.362	0.133	0.128	0.030	1.35	6.33
red_edge	0.028	0.401	0.183	0.177	0.034	1.15	5.78
NIR	0.032	0.558	0.235	0.228	0.041	1.08	5.65

Therefore, all four variables were transformed to standardised gaussian variables by fitting a point model of Gaussian anamorphosis with a number of Hermite polynomials equal to 100. However, to calculate the set of experimental direct and cross-variograms of the gaussian transformed data in a workable computer time, it was necessary to reduce the number of pixels. This was realised by superimposing a regular grid with 1-m mesh on the study area and randomly selecting one point within each cell, so retaining 12974 pixels. The LMC fitted to the set of experimental variograms of the transformed variables consisted of three basic spatial structures: a nugget effect, a spherical model with a range equal to 7.78 m, and a spherical model with a range of 76.59 m. The results of cross-validation (Table 3) were quite good because the mean and variance of standardised error were very close to 0 and 1, respectively, for all variables.

Table 3. The results of cross-validation for fitting of point LMC of the gaussian transformed drone reflectance variables. g before the band name stands for the gaussian transformed drone variable.

Variable	Mean	Variance
g_green	0.0031	1.01
g_red	-0.0083	1.00
g_red_edge	-0.0007	1.07
g_NIR	0.0001	1.06

By summing the structure-specific eigenvalues (data not shown), it was possible to decompose the total spatial variance into three components accounting for 43%, (nugget effect), 43% (short-range) and 14% (long range). These results show a clear prevalence of the variability at short scales, within about 7m, most likely due to the very fine scale (0.07m) of drone data monitoring.

To fuse the drone data with the ground-based data with larger support (1m by 1m), the experimental variograms were regularised on the larger support and then a block LMC was fitted (Fig. 4) including a nugget effect, a spherical model with a range of 10.93 m, and a spherical model with a range of 77.59 m.

Preprints (www.preprints.org) | NOT PEER-REVIEWED | Posted: 11 August 2022 doi:10.20944/preprints202208.0216.v1

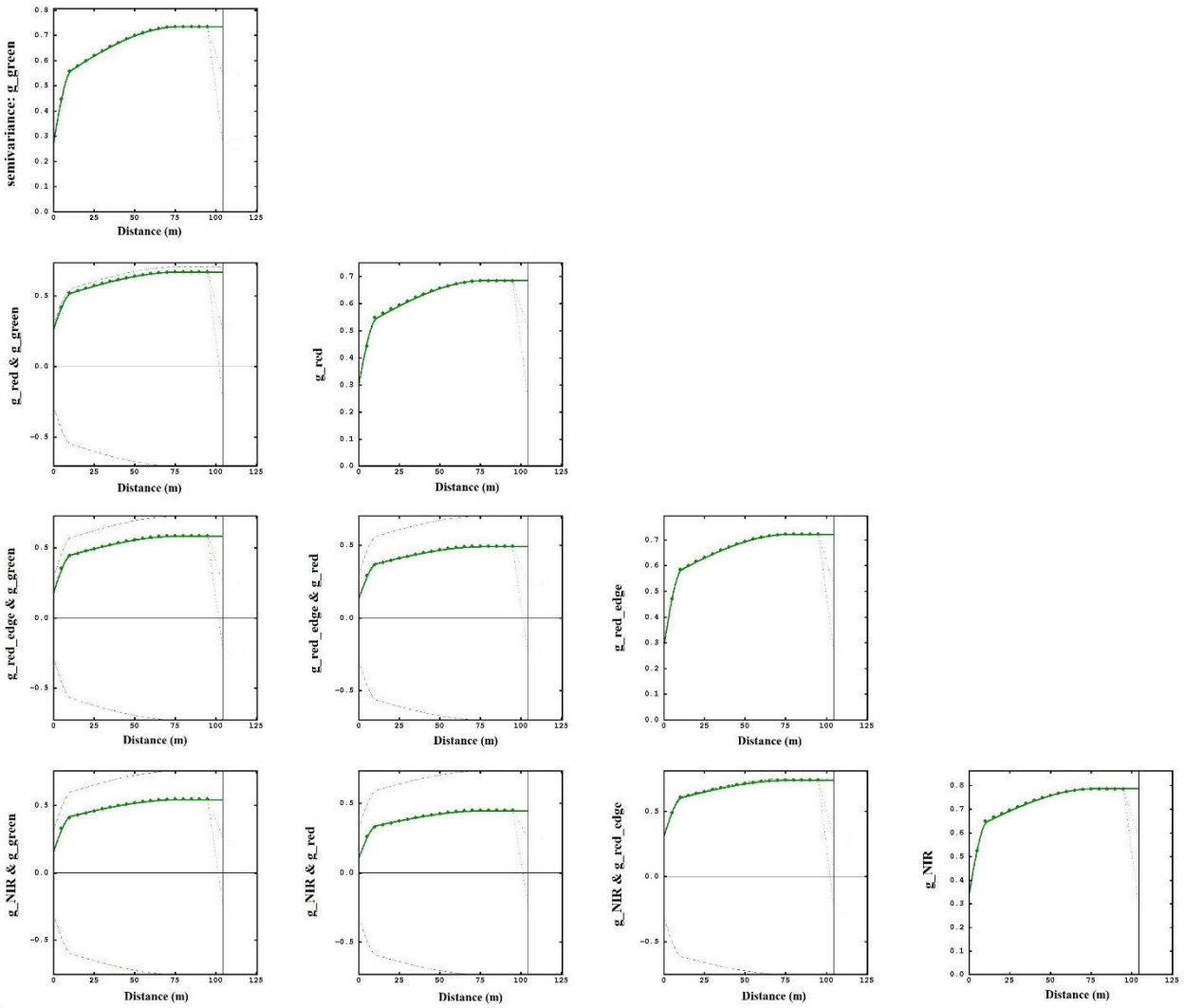

Figure 4. Regularised block LMC of the gaussian transformed drone reflectance variables. Experimental variogram (dots), model (bold line), intrinsic correlation hub (dashed line).

The percentages of total spatial variance explained by the three components were: 41% (nugget effect); 33% (short-range) and 26% (long-range) (data not shown). The effect of the change of support was therefore to leave LMC practically unchanged in the mathematical form of its basic structures, while the proportions of total variance explained by each component were varied. There was a proportional reduction in short-range variability in favour of long-range variability although the error component (nugget effect) remained high. Differently, there was a significant reduction in the total spatial variance from 5.26 for the point model to 2.93 for the block model (about 56 %) as it results from the sum of all respective eigenvalues.

Block LMC was then used in block cokriging to obtain the estimates of drone transformed data both at the nodes of a 1m- mesh grid (auxiliary grid data) and at the locations of the soil samples (sample data), in order to create the complete coregionalization data set including all variables used in data fusion.

3.2. Geostatistical soil data fusion

Table 4 shows the basic statistics of the complete coregionalisation data set. It is worth pointing out that it was preferred to include only the individual variables D1400, D1900

Preprints (www.preprints.org) | NOT PEER-REVIEWED | Posted: 11 August 2022 doi:10.20944/preprints202208.0216.v1

and D2200 in the interpolation process, while the two ratios were calculated subsequently from their estimates.

Table 4. The statistics of the complete coregionaliisation data set. bck before the name of the variable stands for block cokriging estimate.

Variable	Count	Minimum	Maximum	Mean	Std. Dev.	Skewness	Kurtosis
Clay	61	13.34	16.48	14.94	0.72	0.00	2.50
Silt	61	27.53	33.22	30.16	1.38	0.19	2.19
Sabbia	61	51.19	57.98	54.90	1.90	-0.12	1.79
D1400	61	0.05	0.09	0.07	0.01	-0.23	2.73
D1900	61	0.18	0.30	0.24	0.03	-0.56	2.43
D2200	61	0.05	0.07	0.06	0.01	-0.29	3.29
R1	61	0.88	1.61	1.18	0.14	0.30	3.14
R2	61	2.99	5.20	3.94	0.50	0.03	2.46
PC1	61	-1.43	3.58	0.00	0.99	1.72	6.06
PC2	61	-1.75	2.37	0.00	0.99	0.59	2.47
PC3	61	-1.14	2.39	0.00	0.99	1.13	3.13
SIDSAM	61	0.00	0.09	0.03	0.03	0.90	2.82
bck_g_green	61	-2.74	0.29	-1.82	0.50	1.26	6.61
bck_g_red	61	-2.66	0.48	-1.71	0.51	1.35	6.98
bck_g_red_edge	61	-2.42	0.36	-0.93	0.69	-0.18	2.08
bck_g_NIR	61	-2.27	0.98	-0.66	0.76	-0.21	2.19

Furthermore, sand was excluded from the multivariate geostatistical analysis as it was linearly related to clay and silt. Since the variables were expressed in different units and with different magnitudes, and some of them deviated significantly from the Gaussian distribution, it was preferred to apply a Gaussian anamorphosis with 100 Hermite polynomials to all 13 variables.

Given the limited number of samples (61), it was not possible to discover any anisotropy in the spatial variation of the variables. An isotropic LMC was then fitted to the set of direct and cross variograms of the Gaussian transformed variables, comprising the following spatial structures: a nugget effect, a spherical model with a range of 29.89 m and a spherical model with a range of 104.21 (Fig. S1).

Preprints (www.preprints.org) | NOT PEER-REVIEWED | Posted: 11 August 2022 doi:10.20944/preprints202208.0216.v1

(a)

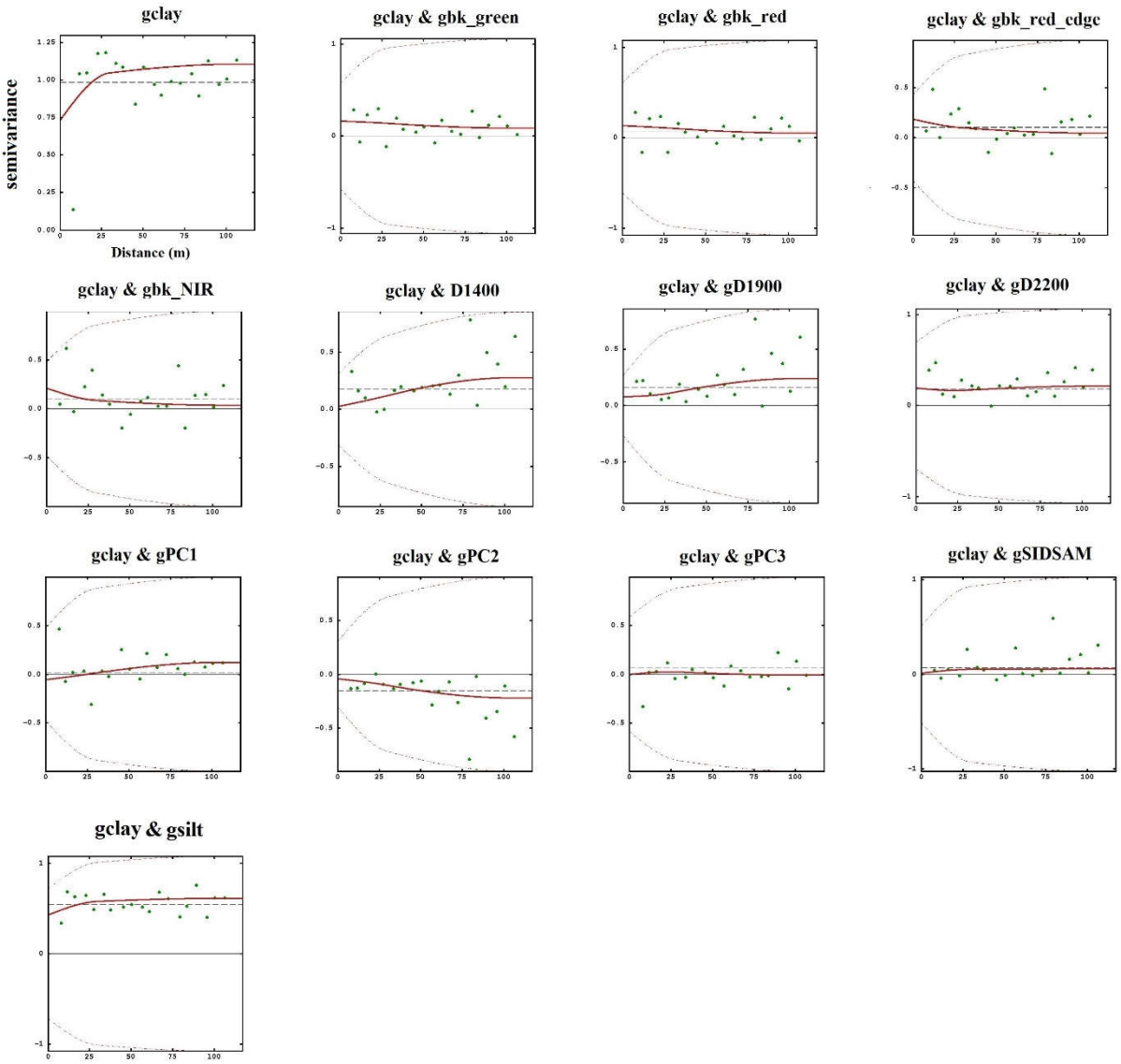

Preprints (www.preprints.org) | NOT PEER-REVIEWED | Posted: 11 August 2022 doi:10.20944/preprints202208.0216.v1

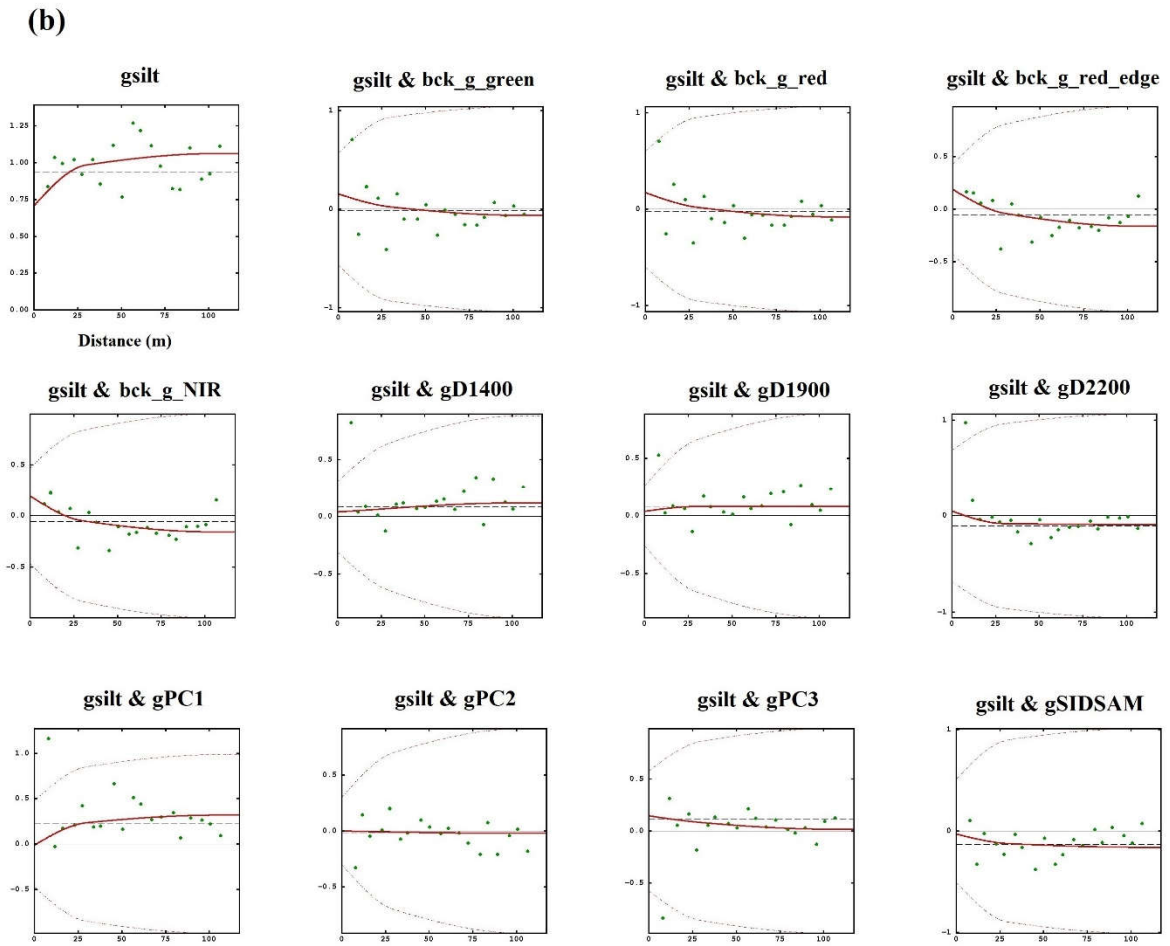

Figure 5. The direct and cross variograms of the two variables: gclay (a) and gsilt (b).

Each of these spatial components explained a percentage of the total variance of 33.7%, 23.6% and 42.7%, respectively. The cross-validation results for the two variables of main interest in this work (gclay and gsilt) were very good (Table 5).

Table 5. The cross-validation results of the two variables (gclay and gsilt) in the data fusion process.

Variable	SE Mean	SE Variance
gclay	-0.009	1.03
gsilt	0.006	1.03

Analysing in particular the direct variogram of gclay and its cross variograms with the remaining variables (Fig. 5a), it can be seen that in the direct variogram, the unstructured component (nugget effect) was high, more than 75 per cent of the total sill. With regard to the cross variograms, by assessing the distance of the model (bold line) from the intrinsic correlation hub (dashed line), an evaluation of the strength of the spatial correlation between the pair of variables is obtained. Intrinsic correlation in fact describes the maximum possible spatial correlation between a pair of variables [26]. It can therefore be noted that these correlations were very low for gclay with all variables, with a partial exception for the positive correlations with gD1400 and gD1900, which was quite expected since gD1400 and gD1900 can be considered as indicators of the specific clay components in the soil.

 doi:10.20944/preprints202208.0216.v1

The same considerations apply largely to gsilt (Fig. 5b). Again, the direct variogram has a high nugget effect (more than 75% of the total sill) and the cross variograms indicate that the spatial correlations with the other variables were generally low, with the exception of the positive correlation with gclay and partly the negative correlation with gSIDSAM and positive correlation with gPC1. The last two spatial correlations indicate that the areas of the field with the highest silt contents were also the most reflective. The general low spatial correlations of the two granulometric components were mostly due to the high nugget effect of both direct variograms, so indicating that soil sampling should be intensified.

It is worth underlining that in the process of data fusion it was not necessary to subject the variograms to regularisation, since all variables considered were defined on the same 1m x 1m size support. Furthermore, the comparison of the block LMC of the drone data alone with the LMC of the complete fusion data set reveals an increase in the range of spatial structures, a proportional reduction in the error component, and a prevalence of the long-range structured component over the short-range one. These results should highlight how modelling of spatial variation depends significantly on the sampling scheme (size, sampling distance, sample localisation) and the measurement support. It is therefore critical in a data fusion process to uniform the supports of all variables used to the same support on which estimates are to be made.

The raw data maps of clay and silt with their respective lower limit and upper limit maps are shown in Fig. 6, so to be able to determine the uncertainty of estimates at each point.

Preprints (www.preprints.org) | NOT PEER-REVIEWED | Posted: 11 August 2022 doi:10.20944/preprints202208.0216.v1

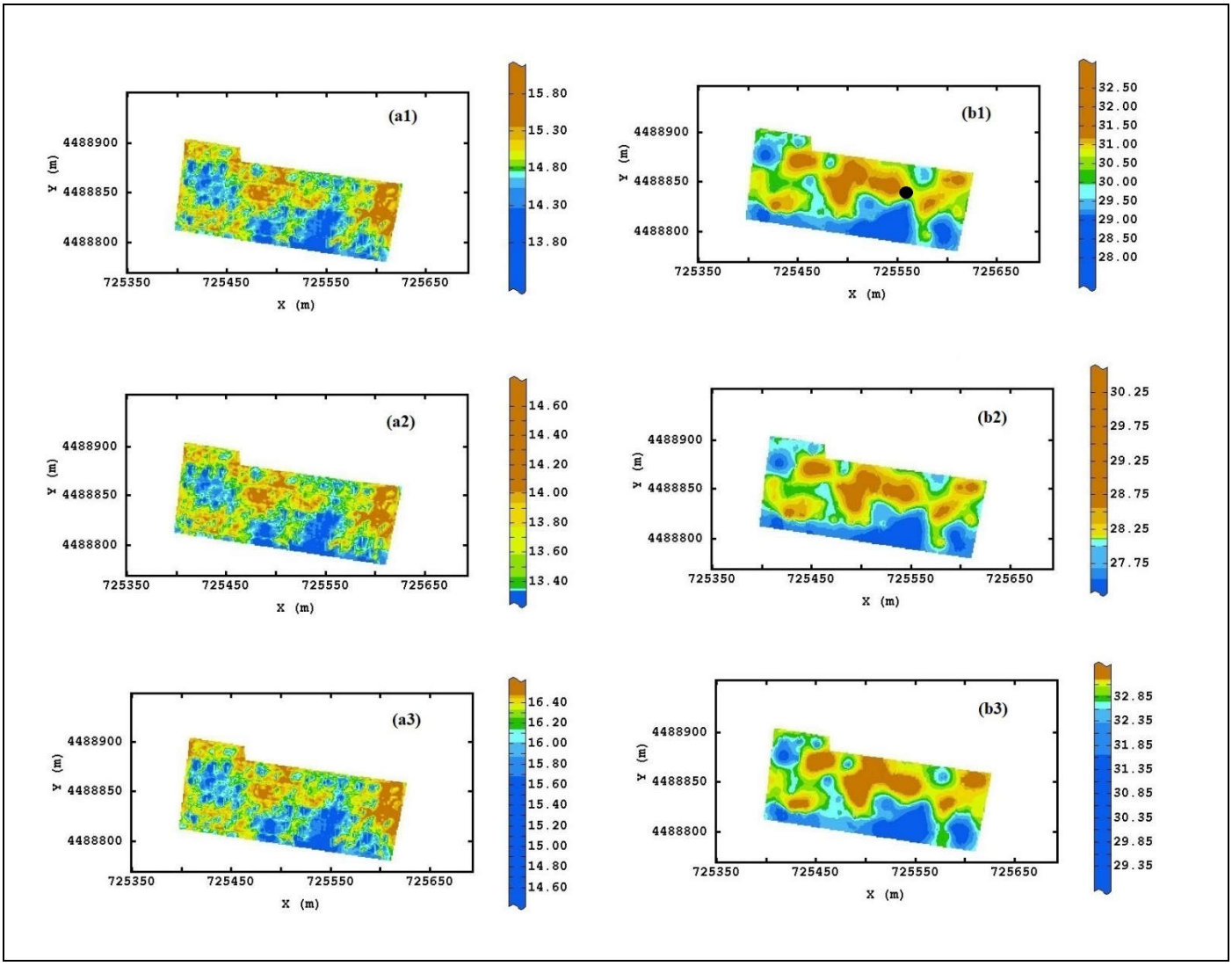

Figure 6. The raw data maps of clay (a1) and silt (b1) with their respective lower limit (a_2, b_2) and upper limit maps (a_3, b_3). In fig. 6b_1 the position of reference spectrum is shown (dot). Colour scale uses isofrequency classes.

The upper and lower limit maps appear very similar to those of the corresponding estimates except in the absolute values, indicating that they reproduce essentially the same spatial dependence structures.

The clay and silt maps show some affinities although the one of clay is noisier, probably due to the low clay content compared to that of silt. The field can then roughly be divided into two parts according to the longer axis: the northern part characterized by a greater proportion of fine component than the southern one. This field partition is also consistent with the sand map drawn from the previous two (Fig. 7), indicating a coarser grain size in the southern part and in the north-western corner.

Preprints (www.preprints.org) | NOT PEER-REVIEWED | Posted: 11 August 2022 doi:10.20944/preprints202208.0216.v1

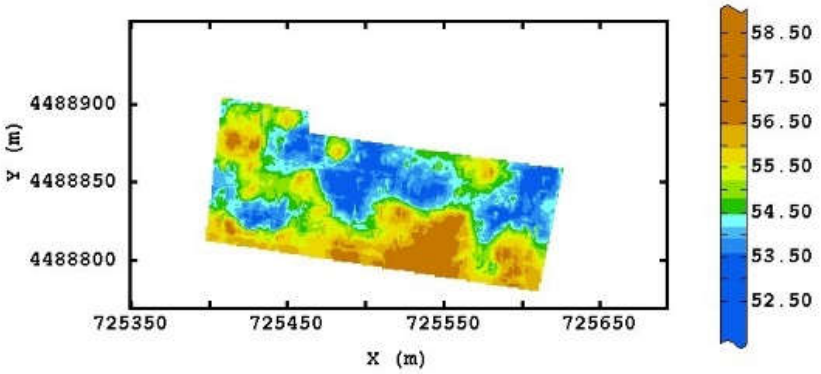

Figure 7. The sand map. Colour scale uses isofrequency classes.

To better characterize the detected within-field homogeneous zones and detail the spatial relationships between the granulometric components and hyperspectral measurements, the maps of D1400, D1900 and D2200 are also shown (Fig. 8).

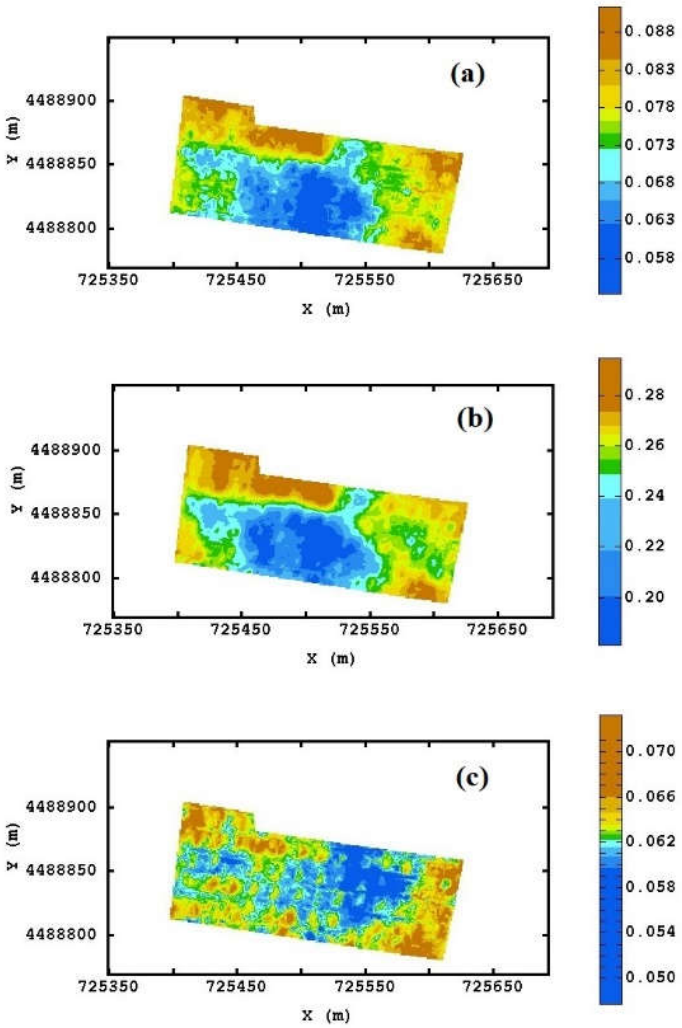

Figure 8. The maps of D1400 (a), D1900 (b) and D2200 (c). The colour scale uses isofrequency classes.

Preprints (www.preprints.org) | NOT PEER-REVIEWED | Posted: 11 August 2022 doi:10.20944/preprints202208.0216.v1

The first two maps correspond to the two clay components called illite (Fig.8a) and montmorillonite (Fig.8b) that look very similar with the lowest D values in the south-west area. The third, representing the clay component called caolinite (Fig.8c), is noisier with the area of the lows shifted more towards the north-east. Also, after normalization of D values with respect to granulometry, the maps of R1 (Fig. 9a) and R2 (Fig. 9b) ratios confirm the geometrical pattern of the illite and montmorillonite clay components. Actually, the ratio maps consistently provide information not only on the spatial distribution of clay content (Fig. 6a), but also on its composition with a prevalence of montmorillonite over illite.

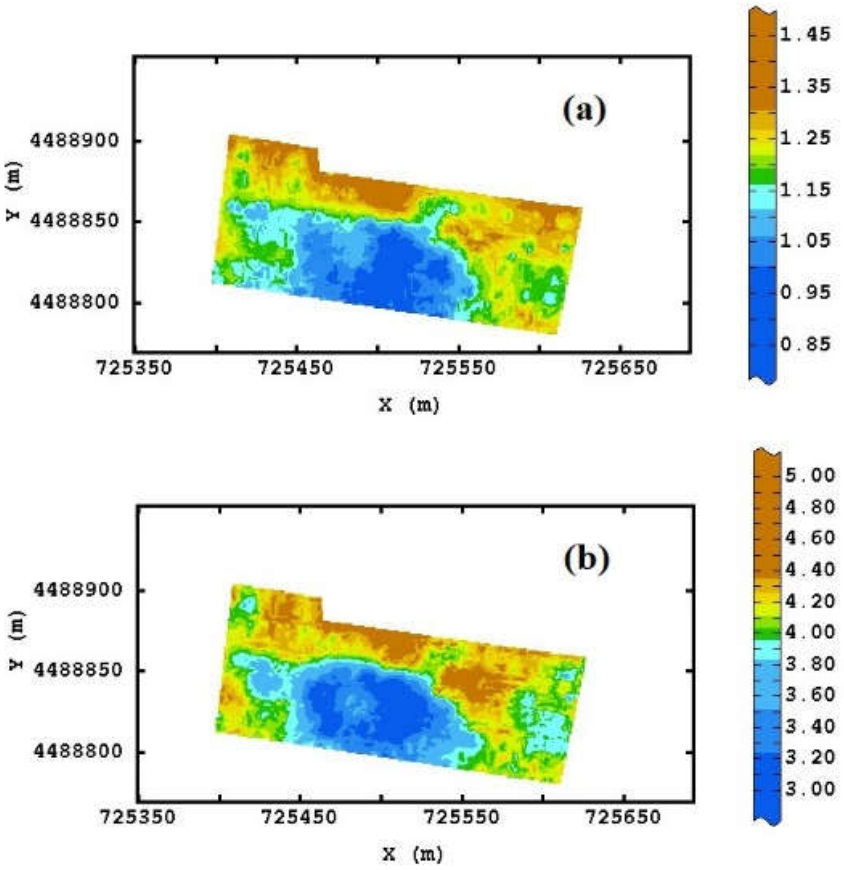

Figure 9. The R1 (a) and R2 (b) ratio maps. The colour scale uses isofrequency classes.

The SIDSAM map (Fig. 10) displays a broad strip in the north-east to south-west direction characterised by the lowest values, which according to the SIDSAM definition are to be interpreted as areas of higher reflectance over the whole spectrum (350 nm-2500 nm range). Radiation reflection/absorption properties in the VIS-NIR-SWIR range depend on multiple factors, among which soil granulometry plays an important role [24]. The SIDSAM lows should therefore mostly correspond to the coarser granulometry areas of the field.

Preprints (www.preprints.org) | NOT PEER-REVIEWED | Posted: 11 August 2022 doi:10.20944/preprints202208.0216.v1

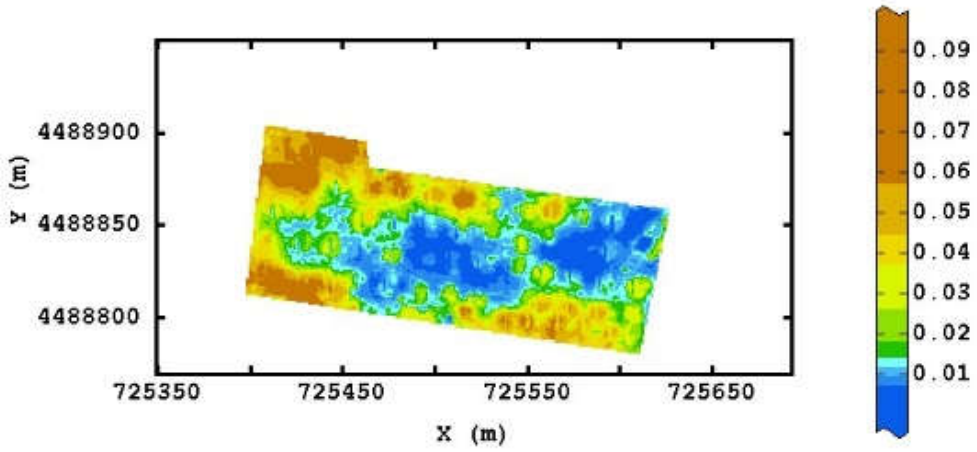

Figure 10. The SIDSAM map. The colour scale uses isofrequency classes. The position of the reference spectrum is indicated (red circle).

Examination of the cross variograms of gSIDSAM with the other variables (Fig. S1) can help us interpret its spatial distribution. gSIDSAM shows negative spatial correlation with gsilt, the radiometric indices over the entire spectrum (gPC1, gPC2 above all, and gPC3), and positive correlation with gD1400 and gD1900. Since SIDSAM is inversely related to soil reflectivity, it can be assumed as a direct indicator of clay content (less reflective) but an indirect indicator of silt content (more reflective).

The location of the absolute most reflective spectrum taken as a reference (Fig. 5b$_1$) seems to be consistent with the above. In fact, it corresponds to a quite high content of silt although not the maximum, since the reflectivity of a soil sample depends on a multitude of physical and chemical properties and not only on the physical size of soil particles.

To synthesise the complex relationships between the spatial structures of the different variables, omitting the factors associated with the nugget effect as they were mostly affected by error, the first two regionalised factors of each spatial structure with eigein value > 1 were retained (Table 6).

Preprints (www.preprints.org) | NOT PEER-REVIEWED | Posted: 11 August 2022 doi:10.20944/preprints202208.0216.v1

Table 6. Structure of the first two regionalized factors at short range (29.89 m) and of the first two regionalized factors at long range (104.91 m) with shown the corresponding loading coefficients, the eigen value and the percentage of explained variance. g before the name of the variable stands for Gaussian transformed variable.

Variable	Scale 29.89 m		Scale 104.21 m	
	F1	F2	F1	F2
gbck_g_green	0.4531	0.2032	0.1001	0.3298
gbck_g_red	0.4037	0.2032	0.0889	0.3472
gbck_g_red_edge	0.3006	0.3592	0.2220	0.4524
gbck_g_NIR	0.2493	0.3674	0.2200	0.4212
gD1400	-0.2316	0.1418	0.5128	-0.2657
gD1900	-0.3275	0.1787	0.5088	-0.1050
gD2200	-0.2114	0.1380	0.1546	-0.0488
gPC1	0.0649	-0.4585	0.1814	-0.3510
gPC2	0.3377	-0.2675	-0.4847	0.1061
gPC3	0.2400	-0.1433	0.1231	0.2514
gSIDSAM	-0.2998	0.4443	0.2209	0.1623
gclay	0.0002	-0.0836	0.0816	-0.1830
gsilt	-0.0885	-0.2489	-0.0161	-0.2170
Eigen Val.	1.4358	1.3355	4.1292	1.9889
Var. Perc.	39.77	37.00	63.26	30.47

On the first factor at short range, which explained about 40% of the variance at this scale, the drone reflectances, which correlated poorly with the other variables, and gF2 weighted mainly and positively, while gD1900 and gSIDSAM weighted negatively. In the light of the interpretation of the variables described above, this factor can be considered an indicator of the soil reflectance as recorded by both multiband and hyperspectral sensors. Unlike on the second short-range factor, which accounts for 37.0% of the variance, gF1 and gSIDSAM weighted mainly negatively and positively, respectively. It may thus be interpreted as an indicator of the radiation absorption by clay.

On the first long-range regionalized factor, which explained more than 63% of the variance at this scale, gD1400 and gD1900 weighted mainly and positively. It can therefore be interpreted as an indicator of the clay content in the forms of illite and montmorillonite. On the second long-range factor, which explained about 30% of the variance, the multiband reflectances from drone weighted positively and at less extent and negatively D1400. Highs in the second factor might be associated with higher silt contents while lows with less clay contents. For this factor it is however more difficult to assign it a unique meaning.

In Fig (11 a_1, a_2), the maps of the two short-range factors are displayed, which are characterised by high level of noise. The highs of the first factor would indicate higher reflectivity areas (greater silt and sand contents), while the highs of the second factor would identify higher radiative absorption areas and then with greater clay contents.

Preprints (www.preprints.org) | NOT PEER-REVIEWED | Posted: 11 August 2022 doi:10.20944/preprints202208.0216.v1

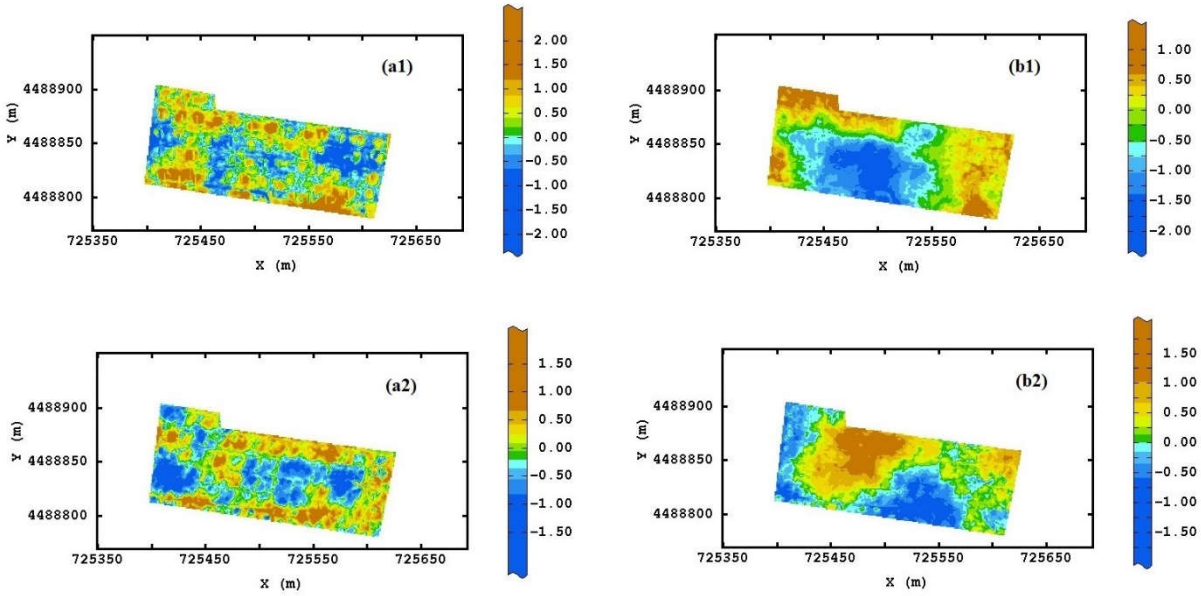

Figure 11. Maps of the first two regionalised factors at short range (a1, a2) and of the first two regionalised factors at long range (b1, b2). The colour scale uses isofrequency classes.

Fig. (11b$_1$) shows the map of the first long-range factor, which almost faithfully reproduces the spatial patterns of the D1400 and D1900 maps. Therefore, it depicts the distribution of clay characterised by a large central southern zone with low contents, while the content increases along the edges of the field except in the south centre, consistently for its two main components. A map of the second long-range factor is shown in Fig. (11b$_2$) where the highs might be attributed to greater silt content and the lows to greater sand content.

It is clear from what has been said above that the soil particle size composition significantly controls the partitioning of this soil into homogenous areas. In particular, based on the first long-range factor, the field could be split into three main areas approximately o equal size defined as low, medium and high level of the content of the finest component of the granulometry (Fig. 12).

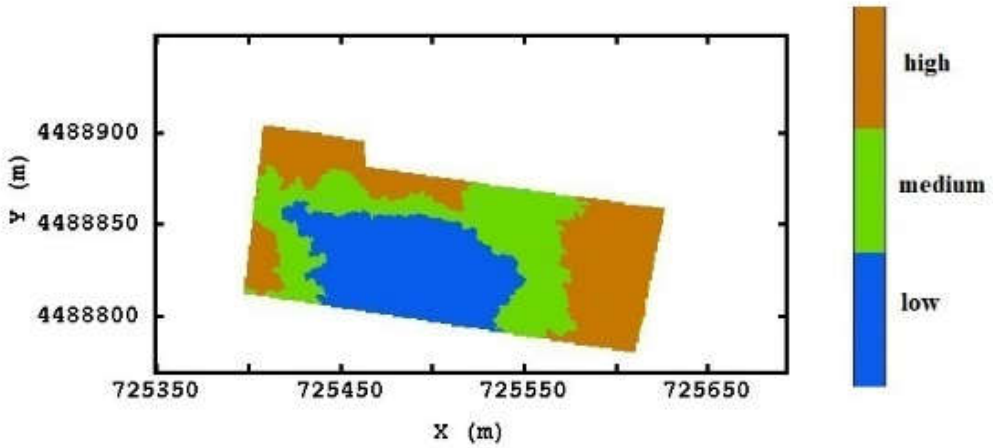

Figure 12. The map of the first long-range factor splitted into three areas of about equal size on the basis of the content of the finest component of granulometry.

 doi:10.20944/preprints202208.0216.v1

Evidently, to arrive at a site-specific agronomic management of the olive grove in terms of mechanical tillage, fertilisation and possible rescue irrigation, further determinations would be needed both on the soil and on the plant. However, the combined use of remote and laboratory sensors can certainly provide an effective support for field partitioning.

5. Conclusions

The objective of this work was to investigate the use of Remote Sensing and in particular of drone data on the soil, to assess spatial variability and then arrive at a partition that could be utilised in differential management. To this end, a geostatistical data fusion approach was defined that could integrate RS data with hyperspectral data and granulometric measurements from the laboratory.

The study has revealed the key advantages of remote sensing especially in PA applications: non destructive method of collecting data on soil parameters; supply of information at fine spatial resolution over the entire field; useful complement to costly and time-consuming sampling. However, it has also shown the disadvantages or limitations of using RS alone whose variables did not show strong spatial relationships with soil parameters. It is then necessary to integrate these measurements with those of other sensors, such as hyperspectral sensors that allow better physical and chemical characterisation, and with direct laboratory determinations of soil properties.

The use of collecting soil samples for laboratory measurements inevitably reduces the size of data, therefore a future challenge is the increase in data volume in addition to an increase in spectral bands through the implementation of a hyperspectral radiometer in remote and/or proximal sensing.

Finally, a crucial issue in which the remote sensing community should be concerned is about scale effects. In fusing RS data with different pixel sizes and with data from various sources, the impact of change of support on prediction and uncertainty should be carefully evaluated since it might significantly affect decision making for example in PA.

Supplementary Materials: Figure S1.

Author Contributions: Conceptualization, A.C. and A.B.; methodology, A.C., A.B., C.R., F.L; formal analysis, A.C., A.B., C.R., F.L.; writing—original draft preparation, A.C..; writing—review and editing, A.C., A.B., C.R.; visualization, A.B.; supervision, A.C.; funding acquisition, A.C. All authors have read and agreed to the published version of the manuscript.

Funding: Project "XylMap - Identification of CoDiRO diffusion dynamics after analysis of progression mechanisms and development of enhanced monitoring and mapping tools and methods" was financed by the Apulia Region (Italy) with reference to DD n. 494 of 14/10/2015 and n. 278 of 9/8/2016 (Cod. A).

Conflicts of Interest: The authors declare no conflict of interest. The funders had no role in the design of the study; in the collection, analyses, or interpretation of data; in the writing of the manuscript; or in the decision to publish the results

References

1. Ge, Y.; Thomasson, J.A.; Ruixiu S. Remote sensing of soil properties in precision agriculture: A review. *Front. Earth Sci.* **2011**, 5, 229–238, doi:10.1007/s11707-011-0175-0.
2. Viscarra Rossel, R.A.; Adamchuk, V.I.; Sudduth, K.A.; McKenzie, N.J.; Lobsey, C. Chapter Five-Proximal Soil Sensing: An Effective Approach for Soil Measurements in Space and Time. *Adv. Agron.* **2011**, *113*, 243–291, doi:10.1016/B978-0-12-386473-4.00005.
3. Mulla D.J. Twenty five years of remote sensing in precision agriculture: Key advances and remaining knowledge gaps. *Biosyst. Eng.* **2013**, *114(4)*, 358–371, doi:10.1016/j.biosystemseng.2012.08.009.
4. Ben-Dor, E. Characterization of Soil Properties Using Reflectance Spectroscopy. *Adv. Agron.* **2011**, *75*, 173–243, doi:10.1201/b11222-31.

5. Lagacherie, P.; Baret, F.; Feret, J.B.; Madeira Netto, J.S.; Robbez-Masson, J.M. Estimation of soil clay and calcium carbonate using laboratory, field and airborne hyperspectral measurements. *Remote Sens. Environ*. **2008,** *112(3)*, 825–835, doi:10.1016/j.rse.2007.06.014.
6. Demattê, J.A.; Alves, M.; Gallo, B.; Fongaro, C; Souza, A.; Romero, D.; Sato, M. Hyperspectral remote sensing as an alternative to estimate soil attributes. *Rev. Cienc. Agron.* **2015**, *46*, 223–232, doi: 10.5935/1806-6690.20150001.
7. von Hebel, C.; Matveeva, M.; Verweij, E.; Rademske, P.; Kaufmann, M. S.; Brogi, C.; Vereecken, H.; Rascher, U. and van der Kruk, J. Understanding soil and plant interaction by combining ground-based quantitative electromagnetic induction and airborne hyperspectral data. *Geophys. Res. Lett.* **2018**, *45*, 7571–7579, doi: 10.1029/2018GL078658.
8. Gomez, C.; Lagacherie, P.; Coulouma, G. Continuum removal versus PLSR method for clay and calcium carbonate content estimation from laboratory and airborne hyperspectral measurements. *Geoderma* **2008**, *148*, 141–148, doi:10.1016/j.geoderma.2008.09.016.
9. Geladi, P.; Macdougall, D.; Martens, H. Linearization and scatter-correction for near-infrared reflectance spectra of meat. *Appl. Spectrosc.* **1985**, *39(3)*, 491–500, doi:10.1366/0003702854248656.
10. Barnes, R.J.; Dhanoa, M.S.; Lister, S.J. Standard normal variate transformation and de-trending of near-infrared diffuse reflectance spectra. *Appl. Spectrosc.* **1989**, *43(5)*, 772–777, doi:10.1366/0003702894202201.
11. Clark, R.N.; Roush, T.L. Reflectance spectroscopy: quantitative analysis techniques for remote sensing applications. *J. Geophys. Res.* **1984**, *89*, 6329–6340. doi:10.1029/JB089iB07p06329.
12. Gaffey, S.J. Spectral reflectance of carbonate minerals in the visible and near infrared (0.35–2.55 m): Calcite, aragonite and dolomite. *Am. Mineral.* **1986**, *71*, 151–162, doi:10.1029/JB092iB02p01429.
13. Chabrillat, S.; Goetz, A.F.H.; Krosley, L.; Olsen, H.W. Use of hyperspectral images in the identification and mapping of expansive clay soils and the role of spatial resolution. *Remote Sens. Environ*. **2002**, *82*, 431–445, doi:10.1016/S0034-4257(02)00060-3.
14. Chatterjee, A.; Michalak, A.M.; Kahn, R.A.; Paradise, S.R.; Braverman, A.J.; Miller, C.E. A geostatistical data fusion technique for merging remote sensing and groundbased observations of aerosol optical thickness. *J. Geophys. Res.* **2010**, *115*, D20207, doi: 10.1029/2009JD013765.
15. Nguyen, H.; Cressie, N.; Braverman, A. Spatial statistical data fusion for remote sensing applications. *J. Am. Stat. Assoc.* **2012**, *107*, 1004–1018, doi: 10.1080/01621459.2012.694717.
16. Castrignanò, A.; Belmonte, A.; Antelmi, I.; Quarto, R.; Quarto, F.; Shaddad, S.; Sion, V.; Muolo, M.R.; Ranieri, N.A.; Gadaleta, G.; et al. A geostatistical fusion approach using UAV data for probabilistic estimation of *Xylella fastidiosa* subsp. *pauca* infection in olive trees. *Sci. Total Environ.* **2021**, *752*, 141814, doi: 10.1016/j.scitotenv.2020.141814.
17. Gotway, C.A.; Young, L.J. Combining incompatible spatial data. *J. Am. Stat. Assoc.* **2002**, *97*, 632–648, doi:10.1198/016214502760047140.
18. Castrignanò, A.; Buttafuoco, G. Data processing: Chapter 3. In *Agricultural Internet of Things and Decision Support for Precision Smart Farming*, 1st ed.; Castrignanò, A., Buttafuoco, G., Khosla, R., Mouazen, A.M., Moshou, D., Naud., O., Eds.; Academic Press: Cambridge, MA, USA, 2020; pp. 139–182.
19. Cressie, N. Change of support and the modifiable areal unit problem. *Geogr. Syst.* **1996**, *3*, 159–180.
20. Goovaerts, P. Sample support. Wyley Stats Ref: Statistics Reference Online; John Wiley & Sons, Ltd. 2016; doi: 10.1002/9781118445112.stat07754.pub2.
21. Harding, B. E.; Deutsch, C.V. Change of Support and the Volume Variance Relation. Available online http://geostatisticslessons.com/lessons/changeofsupport accessed on 13 January 2019.
22. Moshrefi, N. A new method of sampling soil suspension for particle-size analysis. *Soil Sci.* **1993**, *155*, 245–248, doi:10.1097/00010694-199304000-00002.
23. Indorante, S.J.; Follmer, L.R.; Hammer, R.D.; Koenig, P.G. Particle-size analysis by a modified pipette procedure. *Soil Sci. Soc. Am. J.* **1990**, *54*, 560–563, doi:10.2136/sssaj1990.03615995005400020047x.
24. Riefolo, C.; Belmonte, A.; Quarto, R.; Quarto, F.; Ruggieri, S.; Castrignanò, A. Potential of GPR data fusion with hyperspectral data for precision agriculture of the future. *Comput. Electron. Agric.* **2022**, doi: 10.1016/j.compag.2022.107109.
25. Vishnu, S.; Nidamanuri, R.R.; Bremannanth, R. Spectral Material Mapping Using Hyperspectral Imagery: A Review of Spectral Matching and Library Search Methods. *Geocarto Int.* **2013**, *28(2)*, 171–190, doi:10.1080/10106049.2012.665498.
26. Wackernagel, H. *Multivariate Geostatistics: An Introduction with Applications*; Springer Nature: London, UK, 2003; ISBN 139783540441427.
27. Chilès, J.P.; Delfiner, P. *Geostatistics: Modeling Spatial Uncertainty*, 2nd ed.; John Wiley & Sons, Inc.: Hoboken, NJ, USA, 2012, doi:10.1002/9781118136188.
28. Castrignanò, A.; Giugliarini, L.; Risaliti, R.; Martinelli, N. Study of spatial relationships among soil physical-chemical properties using Multivariate Geostatistics. *Geoderma* **2000**, *97*, 39–60, doi:10.1016/S0016-7061(00)00025-2.
29. Goovaerts, P. 1997. Geostatistics for Natural Resources Evaluation; Oxford University Press: New York, NY, USA, p. 483.
30. Rivoirard, J. Which models for collocated cokriging? *J. Math. Geol.* **2001**, *33*, 117–131, doi:10.1023/A:1007530600152.
31. Isaaks, E.H.; Srivastava, R.M. *An Introduction to Applied Geostatistics*, 1st ed.; Oxford University Press: New York, USA, 1989; p. 413.
32. Carroll, S.S.; Cressie, N. A comparison of geostatistical methodologies used to estimate snow water equivalent. *Water Resour. Bull.* **1996**, *32*, 267–278, doi:10.1111/j.1752-1688.1996.tb03450.x.
33. Atkinson, P.M.; Tate, N.J. Spatial Scale Problems and Geostatistical Solutions: A Review. *Prof. Geogr.* **2000**, *52(4)*, 607–623, doi: 10.1111/0033-0124.00250.

34. Journel, A.G.; Huijbregts, C.J. *Mining Geostatistics*; Academic Press: London, UK, 1978; 600p.
35. Armstrong, M. *Basic Linear Geostatistics*; Springer-Verlag: Berlin, Heidelberg, New York, Germany, USA, 1998; p. 22.
36. Castrignanò, A.; Quarto, R.; Venezia, A.; Buttafuoco, G. A comparison between mixed support kriging and block cokriging for modelling and combining spatial data with different support. *Precis. Agric.* **2019**, *20*, 193–213, doi:10.1007/s11119-018-09630-w.
37. Castrignanò, A.; Buttafuoco, G.; Quarto, R.; Vitti, C.; Langella, G.; Terribile, F.; Venezia, A. A Combined Approach of Sensor Data Fusion and Multivariate Geostatistics for Delineation of Homogeneous Zones in an Agricultural Field. *Sensors* **2017**, 17, 2794, doi:10.3390/s17122794.
38. Olea, R.A. *Geostatistical Glossary and Multilingual Dictionary*; Oxford University Press: New York, NY, USA, 1991; p. 192.
39. Myers, D.E. Matrix formulation of Co-Kriging. *Math. Geol.* **1982**, *14*, 249–257, doi: 10.1007/BF01032887.
40. Castrignanò, A.; Costantini, E.; Barbetti, R.; Sollito, D. Accounting for extensive topographic and pedologic secondary information to improve soil mapping. *Catena* **2009**, *77*, 28–38, doi:10.1016/j.catena.2008.12.004.
41. Matheron, G. *Pour une analyse krigeante des données regionalisées*, Technical Report n. 732; Ecole Nationale Superieure des Mines: Paris, Fontainebleau, France, 1982; p. 22.